

1 **Effects of Micro-Arrangement of Solid Particles on PCE**
2 **Migration and Its Remediation in Porous Media**

3 Ming Wu^{1,2}, Jianfeng Wu^{1*}, Jichun Wu^{1**}, and Bill X. Hu²

4

5 ¹Key Laboratory of Surficial Geochemistry, Ministry of Education; Department of
6 Hydrosiences, School of Earth Sciences and Engineering, Nanjing University, Nanjing
7 210023, China

8 ²Institute of Groundwater and Earth Sciences, Jinan University, Guangzhou 510632,
9 China

10 *Correspondence to:* J.F. Wu (jfwu@nju.edu.cn), J. C. Wu (jcwu@nju.edu.cn)

11

12

13

14

15

16

17

18

19

20

21 **ABSTRACT**

22 Groundwater can be stored abundantly in granula-composed aquifers with high
23 permeability. The micro-structure of granular materials has important effect on aquifer
24 permeability; and the contaminant migration and remediation in aquifers is also
25 influenced by the characteristics of porous media. In this study, two different microscale
26 arrangements of sand particles are examined to reveal the effects of micro-structure on
27 the contaminant migration and remediation. With the help of fractal theory, the
28 mathematical expressions of permeability and entry pressure are conducted to delineate
29 granular materials with regular triangle arrangement (RTA) and square pitch arrangement
30 (SPA) at microscale. Using Sequential Gaussian Simulation (SGS) method, a synthetic
31 heterogeneous site contaminated by Perchloroethylene (PCE) is then used to investigate
32 the migration and remediation affected by the two different micro-scale arrangements.
33 PCE is released from an underground storage tank into the aquifer and the surfactant is
34 used to clean up the subsurface environment. Results suggest that RTA not only can
35 cause larger range of groundwater contamination, but also can cause harder remediation
36 for contaminated aquifer. The PCE remediation efficiency of 60.01% -99.78% with a
37 mean of 92.52% and 65.53% -99.74% with a mean of 95.83% are achieved for 200
38 individual heterogeneous realizations based on the RTA and SPA, respectively,
39 indicating that the cleanup of PCE in aquifer with SPA is significantly easier. This study
40 leads to a new understanding of the microstructures of porous media and demonstrates
41 how micro-scale arrangements control contaminant migration in aquifers, which is

42 helpful to design successful remediation scheme for underground storage tank spill.

43 **Keywords:** microscale arrangement; regular triangle; square pitch; contaminant
44 migration and remediation; cumulative PCE removal; macroscopic scale

45

46 **1. Introduction**

47 Groundwater is an essential natural resource for water supply to domestic, agricultural,
48 industrial activities and ecosystem health (Boswinkel, 2000; Valipour, 2012; Valipour,
49 2015; Yannopoulos et al., 2015; Valipour and Singh, 2016). Unfortunately, with the rapid
50 development of economic activities such as mining, agriculture, landfills and industrial
51 activities (Bakshevskaia and Pozdniakov, 2016; Cui et al., 2016; Liu et al., 2016), more
52 and more contaminants released from human activities are contaminating the precious
53 groundwater resource and subsurface environment (Dawson and Roberts, 1997; Liu,
54 2005; Hadley and Newell, 2014; C.Carroll et al., 2015; Essaid et al., 2015; Huang et al.,
55 2015; Liu et al., 2016; Schaefer et al., 2016; Weathers et al., 2016). Out of the
56 contaminants detected in groundwater, dense nonaqueous phase liquids (DNAPLs)
57 such as perchloroethylene (PCE) and other polycyclic aromatic hydrocarbons (PAHs),
58 are highly toxic and carcinogenic (Dawson and Roberts, 1997; Hadley and Newell, 2014).
59 When DNAPLs are released into aquifer from underground storage tank, they will
60 infiltrate through the entire aquifer and form residual ganglia and pools of DNAPLs due
61 to their large densities, high interfacial tension, and low solubility. The residual
62 ganglia and pools of DNAPLs can serve as long-term sources of groundwater
63 contamination that is harmful to subsurface environment and human beings (Bob et al.,

2008; Liang and Lai, 2008; Liang and Hsieh, 2015). Consequently, it is very important to explore DNAPL migration in aquifer and mitigate groundwater contamination by appropriate remediation.

When DNAPL migrates in aquifers at macroscopic scale, the transport properties such as permeability, diffusivity and dispersivity are closely related to the aquifer's microstructures (Yu and Li, 2004; Yu, 2005; Yun et al., 2005; Feng and Yu, 2007; Yu et al., 2009). Therefore, characterizing the effect of microstructures on macroscopic properties is a key point of heterogeneity of porous media. In the classical Kozeny–Carman equation, the permeability K is related to porosity n , surface area S and the Kozeny constant c , where c is affected by the porosity, solid particles and micro geometric structures (Bear 1972; Yu et al. 2009). According to fractal theory, natural porous media can be treated as fractal objects (Pfeifer and Avnir 1983; Katz and Thompson 1985; Krohn 1988). For example, the tortuosity of flow path in porous media is deeply studied by various proposed fractal models (Yu and Cheng 2002; Yu et al. 2009; Cai et al. 2010), indicating the effectiveness of fractal methods compared to experimental observations. Based on fractal concepts, mathematic models are proposed to depict the permeability and invasion of fluids in some special porous media (Yu and Cheng 2002; Yu et al. 2009; Cai et al. 2010). Furthermore, fractal method is also used to explore the effect of microstructure of biological media on associated thermal conductivity while this kind of material has a complex randomly distributed vascular trees structure at microscale (Li and Yu 2013).

In this study, we focus on the effect of micro-arrangement of sand particles on

macroscopic DNAPL migration and associated remediation for underground storage tank spill. With the help of fractal theory, the microstructures of two different microscale arrangements of sand particles are explored. Afterwards, the mathematical relationships between porosity and permeability, entry pressure are derived for regular triangle arrangement (RTA) and square pitch microscale arrangement (SPA). Idealized heterogeneous contaminated site is generated using Sequential Gaussian Simulation (SGS) method. Underground storage tank releases PCE into heterogeneous aquifer composed of granular material and migrates freely. After long time migration, PCE contamination is alleviated using surfactant remediation method. A multicomponent, multiphase model simulator UTCHEM is then used to simulate the entire process of DNAPL migration and remediation. Effects of arrangements of sand particles on migration and remediation of DNAPLs are comparatively analyzed based on the simulations to reveal how the microstructure of porous media controls the contaminant migration and remediation at macroscopic scale.

2. Methodology

2.1 Fractal models of two different microscale arrangements of sand particles

The porous media can be treated as the bundle of tortuous capillary tubes, the relationship between the diameter and the length of capillary tube are (Yu and Cheng, 2002):

$$L_t(\lambda) = \lambda^{1-D_t} L_s^{D_t} \quad (1)$$

107 where L_s is the straight length between the tortuous flow path's end point; λ is the
 108 diameter of capillary tube; D_t is the fractal dimension of tortuosity for porous media,
 109 $1 < D_t < 2$ (Yu and Cheng, 2002).

110 Select an infinitesimal element consisting of a bundle of tortuous capillary tubes
 111 form porous media, the total number of capillary tubes in infinitesimal element can be
 112 calculated by the power-law relation:

$$113 \quad N(L \geq \lambda) = \left(\frac{\lambda_{\max}}{\lambda} \right)^{D_f} \quad (2)$$

114 where D_f is the fractal dimension for pore areas in porous media, $1 < D_f < 2$ (Yu and
 115 Cheng, 2002); λ_{\max} is the maximum diameter of capillary tubes.

116 Afterward, the derivative of Equation (2) can be achieved:

$$117 \quad -dN(L \geq \lambda) = D_f \lambda_{\max}^{D_f} \lambda^{-(D_f+1)} d\lambda \quad (3)$$

118 The total number of capillary tubes in infinitesimal element can be derived from
 119 Equation (3):

$$120 \quad N_i(L \geq \lambda_{\min}) = \left(\frac{\lambda_{\max}}{\lambda_{\min}} \right)^{D_f} \quad (4)$$

121 where λ_{\min} is the minimum diameter of capillary tubes.

122 Dividing Equation (3) by Equation (4) can achieve:

$$123 \quad -\frac{dN(L \geq \lambda)}{N_i} = D_f \lambda_{\min}^{D_f} \lambda^{-(D_f+1)} d\lambda = f(\lambda) d\lambda \quad (5)$$

124 where $f(\lambda)$ is the probability density function, $f(\lambda) = D_f \lambda_{\min}^{D_f} \lambda^{-(D_f+1)}$, it should satisfy

$$125 \quad \int_{-\infty}^{+\infty} f(\lambda) d\lambda = 1 - \left(\frac{\lambda_{\min}}{\lambda_{\max}} \right)^{D_f}. \text{ If } \left(\frac{\lambda_{\min}}{\lambda_{\max}} \right)^{D_f} = 0.$$

126 The probability density function satisfies the relationship:

$$\int_{-\infty}^{+\infty} f(\lambda) d_{\lambda} = 1 - \left(\frac{\lambda_{\min}}{\lambda_{\max}} \right)^{D_f} \quad (6)$$

Considering $\left(\frac{\lambda_{\min}}{\lambda_{\max}} \right)^{D_f} = 0$, the above Equation (6) becomes:

$$\int_{-\infty}^{+\infty} f(\lambda) d_{\lambda} = \int_{\lambda_{\min}}^{\lambda_{\max}} f(\lambda) d_{\lambda} = 1 - \left(\frac{\lambda_{\min}}{\lambda_{\max}} \right)^{D_f} = 1 \quad (7)$$

When fluid flow in capillary tubes, the flow rate Q can be calculated by the Hagen–Poiseuille equation:

$$Q = \frac{\pi^4 \Delta P}{8 \mu L_s} = \frac{\pi \left(\frac{\lambda}{2} \right)^4 \Delta P}{8 \mu L_s} = \frac{\pi \lambda^4 \Delta P}{128 \mu L_s} \quad (8)$$

where μ is fluid's viscosity; ΔP is the pressure gradient across the capillary tube.

The differentiation of flow rate of capillary tubes is (Yu and Cheng, 2002):

$$\begin{aligned} d_q &= [-d_{N(L \geq \lambda)}] \frac{\pi \lambda^4 \Delta P}{128 \mu L_t(\lambda)} = D_f \lambda_{\max}^{D_f} \lambda^{-(D_f+1)} d_{\lambda} \cdot \frac{\pi \lambda^4 \Delta P}{128 \mu L_t(\lambda)} \\ &= \frac{\pi}{128} \frac{\Delta P}{\mu} \frac{D_f \lambda_{\max}^{D_f}}{L_t(\lambda)} \lambda^{3-D_f} d_{\lambda} = \frac{\pi}{128} \frac{\Delta P}{\mu} \frac{D_f \lambda_{\max}^{D_f}}{\lambda^{1-D_f} L_s^{D_f}} \lambda^{3-D_f} d_{\lambda} \\ &= \frac{\pi}{128} \frac{\Delta P}{\mu} \frac{D_f \lambda_{\max}^{D_f}}{L_s^{D_f}} \lambda^{2+D_f-D_f} d_{\lambda} \end{aligned} \quad (9)$$

Integrating the individual flow rate from λ_{\min} to λ_{\max} can achieve the total flow rate (Yu and Cheng, 2002):

$$\begin{aligned} Q &= \int d_q = \int_{\lambda_{\min}}^{\lambda_{\max}} \frac{\pi}{128} \frac{\Delta P}{\mu} \frac{D_f \lambda_{\max}^{D_f}}{L_s^{D_f}} \lambda^{2+D_f-D_f} d_{\lambda} \\ &= \frac{\pi}{128} \frac{\Delta P}{\mu} \frac{D_f}{3-D_f+D_f} \frac{1}{L_s^{D_f}} \lambda_{\max}^{D_f} (\lambda_{\max}^{3-D_f+D_f} - \lambda_{\min}^{3-D_f+D_f}) \\ &= \frac{\pi}{128} \frac{\Delta P}{\mu} \frac{D_f}{3-D_f+D_f} \frac{1}{L_s^{D_f}} \lambda_{\max}^{3+D_f} \left[1 - \left(\frac{\lambda_{\min}}{\lambda_{\max}} \right)^{D_f} \left(\frac{\lambda_{\min}}{\lambda_{\max}} \right)^{3+D_f-2D_f} \right] \end{aligned} \quad (10)$$

Due to $1 < D_f < 2$ and $1 < D_f < 2$, then $3+D_f-2D_f > 0$. Simultaneously, $\left(\frac{\lambda_{\min}}{\lambda_{\max}} \right)^{D_f} \cong 0$,

140 $0 < \left(\frac{\lambda_{\min}}{\lambda_{\max}}\right)^{3+D_t-D_f} < 1$. Therefore, Equation (10) can be simplified as:

$$141 \quad Q = \int d_q = \frac{\pi}{128} \frac{\Delta P}{\mu} \frac{D_f}{3-D_f+D_t} \frac{1}{L_0^{D_f}} \lambda_{\max}^{3+D_t} \quad (11)$$

142 Substituting Darcy's law $Q = \frac{kA\Delta P}{\mu L_0}$ in Equation (11) will obtain the permeability
143 of porous media:

$$144 \quad k = \frac{\pi}{128} \frac{D_f}{3+D_t-D_f} \frac{L_0^{1-D_t}}{A} \lambda_{\max}^{3+D_t} \quad (12)$$

145 To obtain the fractal dimension of tortuosity D_t , the expression of tortuosity (τ)
146 can be obtained from Equation (1):

$$147 \quad \tau = \frac{L_t(\lambda)}{L_s} = \frac{\lambda^{1-D_t} L_s^{D_t}}{L_s} = \left(\frac{L_s}{\lambda}\right)^{D_t-1} \quad (13)$$

148 Then the D_t is given by (Yu and Li, 2001):

$$149 \quad D_t = 1 + \frac{\ln \tau}{\ln\left(\frac{L_s}{\lambda}\right)} \quad (14)$$

150 RTA and SPA are shown in Fig. 1. An equilateral triangle and a square are
151 selected from the two micro-structures as unit cells (Fig. 1a and Fig. 1b). The unit cell
152 of equilateral triangle is composed of three solid particles and the pore among them,
153 while the unit cell of square is composed of four solid particles. For the unit cell of
154 RTA in Fig. 1a, corresponding porosity is given by:

$$155 \quad n = \frac{A_a - \pi R_v^2 / 2}{A_a} \quad (15)$$

156 where n is porosity; A_a is the total area of equilateral triangle; R_v is the average radius
157 of solid particles. The total area of equilateral triangle can be achieved:

$$158 \quad A_a = \frac{\pi R_v^2}{2(1-n)} \quad (16)$$

The side length of the equilateral triangle in Fig. 1a can be calculated as:

$$L_a = R_v \sqrt{\frac{2\pi}{\sqrt{3}(1-n)}} \quad (17)$$

where L_a is the side length.

The area of irregular pore among solid particles is given by:

$$A_{ap} = A_a - \frac{\pi R_v^2}{2} = \frac{\pi R_v^2 n}{2(1-n)} \quad (18)$$

where A_{ap} is the area of pore in the unit cell.

Approximate the pore in the equilateral triangle as a circle, then the maximum diameter of pore can be obtained:

$$\lambda_{max,a} = R_v \sqrt{\frac{2n}{1-n}} \quad (19)$$

where $\lambda_{max,a}$ is the diameter of capillary tube in equilateral triangle. The fluid passes not only the central-pore of the unit cell, but also the gap between adjacent particles. The gap length and the average diameter of capillary tube perpendicular to the plane of equilateral triangle are calculated as follows:

$$\Delta L_a = L_a - 2R_v = R_v \left(\sqrt{\frac{2\pi}{\sqrt{3}(1-n)}} - 2 \right) \quad (20)$$

$$\lambda_a = \frac{\lambda_{max,a} + \Delta L_a}{2} = \frac{R_v}{2} \left(\sqrt{\frac{2n}{1-n}} + \sqrt{\frac{2\pi}{\sqrt{3}(1-n)}} - 2 \right) \quad (21)$$

where ΔL_a is the gap length between solid particles; λ_a is the average diameter of capillary tubes in the equilateral triangle.

Generally, the tortuosity of flow path in porous media is the ratio of the length of tortuous flow path to the straight length of flow path along the flow direction (Taiwo et al., 2016):

$$\tau = \frac{L_t}{L_s} \quad (22)$$

where L_t is the length of tortuous flow path; and L_s is the straight length of flow path along the flow direction.

For the flow path shown in Fig. 1a, the L_t and L_s respectively are:

$$L_t = (h_o - R_v) + \frac{\pi R_v}{2} = R_v \left(\sqrt{\frac{\sqrt{3}\pi}{2(1-n)}} + \frac{\pi}{2} - 1 \right) \quad (23)$$

$$L_s = h_o = R_v \sqrt{\frac{\sqrt{3}\pi}{2(1-n)}} \quad (24)$$

where h_o is the altitude of the equilateral triangle, $h_o = \frac{\sqrt{3}}{2} L_a = R_v \sqrt{\frac{\sqrt{3}\pi}{2(1-n)}}$.

Consequently, the tortuosity of RTA is yielded:

$$\tau = \frac{L_t}{L_s} = 1 + \frac{\frac{\pi}{2} - 1}{\sqrt{\frac{\sqrt{3}\pi}{2(1-n)}}} \quad (25)$$

The D_f is determined using Sierpinski gasket (Fig. 2) in fractal theory (Yu and Cheng, 2002). The shaded area represents solid of porous media and the white area represents pore. The pore area fractal dimension in Figs. 2a-c are 0.000, 1.000 and 1.594, respectively ($1 = L_a^{D_f} = 2^{D_f}$, $3 = L_a^{D_f} = 3^{D_f}$, $13 = L_a^{D_f} = 5^{D_f}$). Based on the Sierpinski gasket, the dimensionless pore area in RTA (Fig. 1a) is approximated as:

$$A_{apd} = (L_a^+)^{D_f} \quad (26)$$

where A_{apd} is the dimensionless pore area of RTA; $L_a^+ = L_a / \lambda_{min}$. Equation (26) can be solved to achieve D_f :

$$D_f = \frac{\ln A_{apd}}{\ln L_a^+} \quad (27)$$

197 The porosity equals to the ratio of the dimensionless pore area of RTA (A_{apd}) to
 198 the dimensionless total area of RTA (A_a^+):

$$199 \quad n = \frac{A_{apd}}{A_a^+} \quad (28)$$

$$200 \quad \text{where } A_a^+ = \frac{A_a}{\pi \lambda_{\min}^2 / 4} = \frac{\frac{\pi R_v^2}{2(1-n)}}{\pi \frac{\lambda_{\min}^2}{4}} = \frac{2R_v^2}{\lambda_{\min}^2} \frac{1}{1-n} = \frac{(d^+)^2}{2} \frac{1}{1-n}; d^+ = \frac{2R_v}{\lambda_{\min}} \therefore L_a^+ = \sqrt{A_a^+}.$$

201 From Equation (28), the dimensionless pore area of RTA (A_{apd}) is given by:

$$202 \quad A_{apd} = n \cdot A_a^+ \quad (29)$$

203 The dimensionless total area of RTA (A_a^+) can be written as:

$$204 \quad A_a^+ = (L_a^+)^2 \quad (30)$$

205 Afterward, L_a^+ is calculated as:

$$206 \quad L_a^+ = \sqrt{A_a^+} = \sqrt{\frac{(d^+)^2}{2} \frac{1}{1-n}} = d^+ \sqrt{\frac{1}{2(1-n)}} \quad (31)$$

207 Substituting Equation (29) and Equation (31) into Equation (27) will derive D_f of
 208 RTA:

$$209 \quad D_f = \frac{\ln A_{apd}}{\ln L_a^+} = \frac{\ln(n \cdot A_a^+)}{\ln(\sqrt{A_a^+})} = 2 + \frac{\ln(n)}{\ln(\sqrt{A_a^+})} = 2 + \frac{\ln(n)}{\ln(d^+ \sqrt{\frac{1}{2(1-n)}})} \quad (32)$$

210 For the unit cell of square shown in Fig. 1b, the porosity is:

$$211 \quad n = \frac{A_b - \pi R_v^2}{A_b} \quad (33)$$

212 where A_b is the total area of the square. Equation (33) can also be expressed as the
 213 area of unit cell:

$$214 \quad A_b = \frac{\pi R_v^2}{1-n} \quad (34)$$

Again, the side length of the square is:

$$L_b = \sqrt{A_b} = R_v \sqrt{\frac{\pi}{1-n}} \quad (35)$$

Consequently, the area of irregular pore in the square is given by:

$$A_{bp} = A_b - \pi R_v^2 = \frac{n\pi R_v^2}{1-n} \quad (36)$$

where A_{bp} is the area of pore in the square.

Approximate the pore as a circle and obtain corresponding maximum diameter:

$$\lambda_{max,b} = 2R_v \sqrt{\frac{n}{1-n}} \quad (37)$$

where $\lambda_{max,b}$ is the maximum diameter of capillary tube perpendicular to the plane of the square. Similarly, fluid flows through the central-pore in the square and the gap between adjacent particles. As a result, the gap and average diameter of capillary tube are expressed as:

$$\Delta L_b = L_b - 2R_v = R_v \left(\sqrt{\frac{\pi}{1-n}} - 2 \right) \quad (38)$$

$$\lambda_b = \frac{\lambda_{max,b} + \Delta L_b}{2} = \frac{R_v}{2} \left(2\sqrt{\frac{n}{1-n}} + \sqrt{\frac{\pi}{1-n}} - 2 \right) \quad (39)$$

where ΔL_b is the gap length between the adjacent two solid particles; λ_b is the average diameter of capillary tube.

For the tortuous flow path in Fig. 1b, the L_t and L_s respectively are given by:

$$L_t = \Delta L_b + \pi R_v = R_v \left(\sqrt{\frac{\pi}{1-n}} - 2 + \pi \right) \quad (40)$$

$$L_s = L_b = R_v \sqrt{\frac{\pi}{1-n}} \quad (41)$$

Afterward, the tortuosity of SPA yields:

$$\tau = \frac{L_t}{L_s} = 1 + \frac{\pi \cdot 2}{\sqrt{\frac{\pi}{1-n}}} \quad (42)$$

The procedure of deriving D_f of SPA is similar to the procedure of calculating D_f of RTA. Similarly, the D_f and porosity of SPA (Fig. 1b) are given by:

$$D_f = \frac{\ln A_{bpd}}{\ln L_b^+} \quad (43)$$

$$n = \frac{A_{bpd}}{A_b^+} \quad (44)$$

where A_{bpd} is the dimensionless pore area of SPA; $L_b^+ = L_b / \lambda_{min}$, A_b^+ is the

$$\text{dimensionless total area of SPA, } A_b^+ = \frac{A_b}{\pi \lambda_{min}^2 / 4} = \frac{\frac{\pi R_v^2}{4}}{\pi \frac{\lambda_{min}^2}{4}} = \frac{4R_v^2}{\lambda_{min}^2} \frac{1}{1-n} = (d^+)^2 \frac{1}{1-n}.$$

The dimensionless pore area of SPA (A_{bpd}) can be yielded from Equation (44):

$$A_{bpd} = n \cdot A_b^+ \quad (45)$$

L_b^+ can be calculated as:

$$L_b^+ = \sqrt{A_b^+} = \sqrt{(d^+)^2 \frac{1}{1-n}} = d^+ \sqrt{\frac{1}{1-n}} \quad (46)$$

Substituting Equation (45) and Equation (46) into Equation (43), D_f of SPA can be derived:

$$D_f = \frac{\ln A_{bpd}}{\ln L_b^+} = \frac{\ln(n \cdot A_b^+)}{\ln(\sqrt{A_b^+})} = 2 + \frac{\ln(n)}{\ln(\sqrt{A_b^+})} = 2 + \frac{\ln(n)}{\ln(d^+ \sqrt{\frac{1}{1-n}})} \quad (47)$$

The entry pressure of tortuous capillary tube (P_c) is defined by Yong-Laplace equation as follows (Ahn and Seferis, 1991):

$$P_c = \frac{\omega}{\lambda} \frac{1-n}{n} \quad (48)$$

where P_c is the entry pressure; λ is the diameter of capillary tube; ω equals to $F \sigma \cos \theta$

252 in which θ is the contact angle between fluid and solid, σ is the surface tension of the
253 wetting fluid, and F is the form factor depending on the capillary tube alignment and
254 the flow direction.

255 **2.2 Dealing with the heterogeneity of porous media**

256 In this study, Sequential Gaussian Simulation (SGS) is used to generate random
257 realization of heterogeneous porosity field. SGS is a stochastic simulation method
258 combining sequential principle and Gaussian method. It assumes variable fit to Gaussian
259 random field. The gauss distribution function is constructed at the each simulated spatial
260 location based on the characteristics of variation function, afterward, randomly selects a
261 value as the variable at the location. In SGS method, observation data are transformed to
262 Gaussian distribution or normal distribution. Based on current sample data, the
263 conditional probability distribution of points to be simulated is calculated by SGS
264 method and then simulation is performed based on semivariogram model. Each
265 simulated value, together with measured data and previous simulation data, becomes the
266 conditional data set for the next step. As simulation proceeds, the conditional data set
267 increases. Pervious researches suggested 50–400 realizations are required to obtain a
268 statistically stable mean realization (Eggleston et al., 1996; Hu et al., 2007).

269 **2.3 Modeling PCE migration and its remediation**

270 The DNAPL migration and remediation are modeled using a multi-component,
271 multi-phase, and multi-composition of contaminant-transport processes simulator named

UTCHEM (University of Texas Chemical Compositional Simulator) (Delshad et al., 1996). As an extension to Delshad's work, UTCHEM was developed by University of Texas as a comprehensive and practical tool. In numerous applications, UTCHEM has proved to be particularly useful and has been a popular multi-phase flow and multi-constituent, reactive transport model used widely in groundwater simulations. UTCHEM account for chemical, physical and biological reactions, complex non-equilibrium sorption, decay and geochemical reactions and surfactant-enhanced solubilization and mobilization of DNAPLs, moreover, heterogeneous properties of porous media is addressed. As a result, UTCHEM has been adapted for a variety of environmental applications such as surfactant-enhanced aquifer remediation (SEAR). In this study, DNAPL migration and remediation for cleaning up DNAPL contamination in idealized heterogeneous site are simulated by UTCHEM.

3. Application to a synthetic heterogeneous PCE contaminated site

3.1 Site description

The idealized domain synthetic application is a two-dimensional confined aquifer saturated by water (Fig. 3). The length, width and depth of aquifer are 101 m, 25 m and 25 m, respectively. Idealized aquifer is discretized into 101 grids horizontally and 25 layers vertically (Fig. 3b). The spacing of each grid is uniformly 1 m along x and z directions, and the longitudinal and transverse dispersivities are set as to 1.0 m and 0.1 m, respectively. Horizontal and vertical correlation length values is 5 m. The top and bottom borders of aquifer are defined as no-flow boundaries, while the left and right

293 borders are defined as constant potential boundaries to create a groundwater flow from
294 left to right under a low hydraulic gradient of 0.005 m/m (Liu et al., 2003; Liu, 2005; Qin
295 et al., 2007). The porous media of idealized aquifer is assumed to be heterogeneous and
296 mixed by different grades of sands.

297 The porosity of aquifer is assumed spatially and uniformly distributed with average
298 value of 0.220 and standard deviation of 0.060. In this study, porosity follows normal
299 distribution and its standard deviation (SD) represents the enhanced geological
300 heterogeneity. 200 realizations porosity field are generated using Sequential Gaussian
301 Simulation (SGS). One of the 200 realizations of heterogeneous field is shown in Fig. 4a.
302 Simultaneously, statistical assessment is taken on the individual realization of porosity
303 field and corresponding histograms are shown in Fig. 4b. We can find the frequency of
304 the individual realization of porosity field is close to normal distribution, which conform
305 to the fact that most characteristic of natural aquifer can be expressed as normal
306 distribution (Montgomery et al, 1987). Based on the heterogeneous porosity field, the
307 fractal dimension of tortuosity D_t , the fractal dimension for pore areas D_f and the
308 diameter of capillary tube in porous media, permeability is obtained by the Equation
309 (12). Fig. 4c shows the individual heterogeneous permeability field selected from the
310 200 realizations of RTA, besides, the result of associated frequency analysis is shown in
311 Fig. 4d. The permeability field fits the lognormal distribution obviously, which has been
312 presented by many researches that the parameter of aquifer penetrability is lognormal
313 distribution field (Montgomery et al., 1987; Veneziano and Tabaei, 2004). Compared to
314 histogram of porosity field in Fig. 4b, the shape of permeability is similar. The individual

heterogeneous permeability field of SPA is shown in Fig. 4e. Corresponding frequency analysis of SPA reveals the permeability field is lognormal distribution, while some difference appears compared with RTA (Fig. 4f). The average permeability of individual realization of RTA is $2.012 \times 10^{-12} \text{ m}^2$ and the average permeability of individual realization of SPA is $1.618 \times 10^{-12} \text{ m}^2$. For 200 realizations, the average permeability of RTA and SPA are $2.120 \times 10^{-12} \text{ m}^2$ and $1.706 \times 10^{-12} \text{ m}^2$, indicating the permeability of RTA is bigger than SPA slightly.

The average pore diameters of two different microscale arrangements of particles are derived using corresponding fractal models. In detail, average diameter of RTA is calculated by Equation (21) and average diameter of SPA is calculated by Equation (39). Consequently, the entry pressure of the two kinds of microscale arrangements can be obtained by Equation (48), respectively. The individual entry pressure fields of two microscale arrangements and associated frequency analysis are shown in Figs. 4g-j. From the frequency of entry pressure in Fig. 4h and Fig. 4j, the entry pressures of both RTA and SPA are the lognormal distributions. However, the average entry pressure of individual realization of RTA is 1.980 kPa, while the average entry pressure of SPA is 1.481 kPa. For 200 realizations of entry pressure field, the average entry pressure of RTA is 1.922 kPa and the average entry pressure of SPA is 1.442 kPa. The differences of average entry pressure and the entry pressure distributed range between RTA and SPA imply the micro-structure of aquifer has effect on the macroscopic characteristics.

The purpose of this study is to explore the effects of micro-structure of aquifer on DNAPL migration and remediation. A PCE spill event (the leaking of underground

337 storage tank) occurs on the top of the aquifer and a surfactant remediation is desired to
338 clean up the contaminated aquifer. The total duration of 300 days is divided into four
339 stages: (1) 300 m³PCE is released from underground storage tank into aquifer at the top
340 layer of spill position shown in Fig. 3a during 0~30 days; (2) PCE migrates in aquifer
341 freely during 30~100 days; (3) surfactant is injected into aquifer during 100~150 days;
342 and (4) water flushing during 150~300 days. In the first stage, PCE is released as a point
343 pollution source in the center grid block at the top layer of the aquifer, which spill is at a
344 constant rate of 10 m³/day. After PCE coming into heterogeneous aquifer, PCE is
345 migrating freely under the effects of gravity and the natural hydraulic gradient condition.
346 The PCE not only migrates downward through the aquifer, but also can be trapped by
347 capillary forces as residual ganglia and globules. During the long-term PCE migration
348 period, PCE is contaminating groundwater and expanding plume. To clean up the
349 contaminated aquifer, 4% surfactant solution is injected into aquifer through the two
350 injection wells (Fig. 3b) at a constant rate of 80 m³/day, simultaneously, contaminated
351 groundwater is extracted through production well at constant rate of 160 m³/day.
352 Surfactant can reduce the interfacial tension between DNAPL and aqueous phase to
353 promote solubilization and mobilization of DNAPL in aquifer. After surfactant injection,
354 the contaminated aquifer is flushed by water over a long time of 150 days. Based on the
355 distributions of porosity, permeability and entry pressure of two microscale arrangements,
356 the entire PCE migration and remediation process is simulated by a multicomponent,
357 multiphase model simulator UTCHEM (Delshad et al., 1996). The parameters used in
358 simulation are listed in Table 1. Simulation results of two different microscale

arrangements are compared to reveal the effect of microstructure on the DNAPL migration and remediation.

3.2 Results and discussion

3.2.1 PCE migration and its remediation based on single realizations

The simulation results of PCE migration for individual realization of porosity field for RTA are shown in Fig. 5a-f. When PCE is released into aquifer into aquifer at the top layer of spill position, PCE almost infiltrates vertically under the effect of gravity force (Fig. 5a). Due to the heterogeneity of aquifer, some preferential flow appears and PCE plume becomes irregular (Fig. 5b). After 30 days, PCE plume almost touches the bottom of aquifer (Fig. 5c). When the PCE leakage is stopped, PCE continues to migrate freely in aquifer for 70 days (Fig. 5d-f). The released PCE is migrating downward and entrapped by capillary forces as residual ganglia and globules. Heterogeneity of aquifer makes PCE migrate along preferential pathway. When PCE plume touches the zones of low permeability and high entry pressure, it will bypass these zones and migrate continuously, which leads to an increasing variability in PCE distribution. After PCE plume reaches the bottom of aquifer, PCE begins accumulate and form contaminant pool at the bottom. At t=100 days, A PCE pool has been formed at the bottom of aquifer, moving toward the right boundary.

Figs. 6a-f show the simulated PCE saturation for individual realization of porous media for SPA during migration period. Under the effects of gravity force and natural hydraulic gradient, PCE is migrating and spreading contaminant plume. Heterogeneity

380 of aquifer significantly changes the migration paths and leads to irregular morphology
381 of the PCE plume (Figs. 6a-c). However, due to the different micro-arrangement of
382 aquifer, the entry pressure field also is different which leads to some differences. After
383 the PCE injection, the simulated PCE saturation in Figs. 6d-f indicates that further
384 trapping and spreading of the PCE occurs during this period. Compared with the
385 simulation results of RTA in Fig. 5, the PCE plume slightly seems similar in Fig. 6.
386 Moreover, PCE infiltrate more quickly in porous media of RTA in Fig. 5. After 70 days,
387 PCE plume has touched the bottom for RTA (Fig. 5e), while PCE plume based on SPA
388 still keeps a significant distance from bottom (Fig. 6e).

389 To clean up the DNAPL, 4% surfactant solution is injected through two injection
390 wells at a constant rate of 80 m³/day over 50 days to evaluate the effectiveness of
391 surfactant flushing. Afterwards, following water-flush is applied during 150~300 day.
392 The location of injection wells and production well are presented in Fig. 3b. The
393 production well is rightly installed at the location of the PCE spill position and two
394 injection wells are located 39 m to the left and right of the production well. Figs. 5g-l
395 shows the PCE remediation results of individual realization for RTA. During the early
396 remediation period, the effect of cleaning up DNAPL is not yet apparent (Figs. 5g-i).
397 When the water flushing begins, the surfactant solution circulates throughout the
398 contaminated aquifer (Figs. 5j-l). At t=200 days, there has been 237.01 m³ PCE
399 removal from contaminated aquifer, occupying 79.00% of the total released PCE (Fig.
400 5j). As time goes on, 268.30 m³ PCE is removed from aquifer and remediation
401 efficiency reaches 89.43%.

402 The same surfactant remediation is also conducted for individual realization of
 403 porous media for SPA. Compare with the remediation for RTA, the remediation effect
 404 is more apparent for SPA (Figs. 6g-l). As the remediation processes, more DNAPL is
 405 removed and less DNAPL is remained as small contaminant pools at the bottom of
 406 aquifer. At $t=200$ day, 267.68 m^3 PCE is removed from contaminated aquifer,
 407 corresponding remediation efficiency rise to 89.23%. At $t=300$ day, 285.32 m^3 PCE is
 408 cleaned up and remediation efficiency reaches 95.11%. From results of remediation, it
 409 is obvious that microstructure has effect on remediation of macroscopic scale aquifer.
 410 Results suggest contaminated aquifer of RTA is hard to clean up by surfactant
 411 remediation while SPA can improve DNAPL remediation efficiency.

412 **3.2.2 PCE migration and SGS realizations**

413 PCE migration and remediation processes are simulated for 200 realizations of
 414 porosity field for porous media of RTA and SPA. The variations of contaminant mass,
 415 the ganglia-to-pool ratio (GTP) and moments of PCE plume versus time are presented
 416 in Figs. 7a-h. During 0~30 day, the PCE in aquifer increases linearly at a constant rate
 417 of $10 \text{ m}^3/\text{day}$ (Fig. 7a), which corresponding to contaminant spill stage. Afterward, PCE
 418 volume keep constant during the second stage ranged 30~100 day, while PCE in
 419 aquifer is reduced when surfactant is injected into aquifer. After surfactant and water
 420 flushing the contaminated aquifer, most DNAPL is cleaned up. The residual DNAPL
 421 mass remained in aquifer of 0.67 m^3 - 119.89 m^3 with a mean of 22.42 m^3 and 0.79
 422 m^3 - 103.33 m^3 with a mean of 12.51 m^3 are achieve for 200 individual heterogeneous

423 realizations based on the RTA and SPA, respectively. The average remediation
424 efficiency of SPA is undoubtedly higher than RTA, indicating the aquifer of SPA is easier
425 to clean up. PCE plume architectures are quantified by measuring the ganglia-to-pool
426 ratio (GTP) in Fig. 7b. Over entire periods, curves of GTP value appear obvious
427 oscillations. Surfactant has the ability of promoting solubilization and mobilization of
428 DNAPL can reduce GTP value. As a result, when surfactant is injected at $t=100$ day, the
429 GTP value reduces quickly. When surfactant injection is end and water flushing begins,
430 the GTP value increases with steep flank slope. At last, GTP values reach 0.10-0.41 with
431 a mean of 0.21 and 0.15-0.42 with a mean of 0.28 for 200 individual heterogeneous
432 realizations based on the RTA and SPA, respectively.

433 Fig. 7c shows cumulative PCE removal from contaminated aquifer versus flushing
434 time for RTA and SPA. During the surfactant injection period ranged 100~150 day, the
435 DNAPL removal is not apparent, However, DNAPL is removed effectively and quickly
436 during water flushing period. Through long time remediation, the removal PCE from
437 contaminated aquifer reach 179.89 m^3 - 298.98 m^3 with a mean of 277.29 m^3 and 196.45
438 m^3 - 298.87 m^3 with a mean of 287.21 m^3 for 200 realizations based on RTA and SPA,
439 respectively. Average remediation efficiency of SPA (95.83%) is obvious higher than
440 average remediation efficiency of RTA (92.52%).

441 Fig. 7d shows the GTP value as a function of cumulative PCE removal for
442 contaminated aquifer. The GTP remains at a relatively low level before 30% of the
443 DNAPL is removed from aquifer. When 40% of the total 300 m^3 PCE are removed, GTP
444 values are increasing and corresponding curves appear a wave crest because the high

445 saturation zone of PCE plume are dissolved and turned into ganglia state. After the wave
446 crest, the GTP values decline quickly with steep flank slope due to PCE ganglia removal
447 through water flushing. At last, GTP values increase at the end of remediation process for
448 200 realizations, indicating most of PCE is removed and most of residual PCE turn to
449 ganglia state.

450 For the center of PCE plume in horizontal axis, associated variations versus time are
451 similar for 200 realizations based on RTA and SPA (Fig. 7e). Significantly, the PCE
452 plume vertical infiltration rate in aquifer of RTA is slightly faster than PCE infiltration in
453 aquifer of SPA for 200 realizations (Fig. 7f). Simultaneously, the second PCE plume
454 moments in horizontal direction of RTA are different from SPA (Fig. 7g). After PCE
455 migration at natural condition at 100 day, the second PCE plume moments in horizontal
456 direction are 10.61 m²-40.50 m² with a mean of 21.51 m² and 10.99 m²-36.38 m² with a
457 mean of 20.75 m² for 200 realizations based on RTA and SPA, respectively. At t=300 day,
458 the second PCE plume moments in horizontal direction change to 0.81 m²-34.88 m² with
459 a mean of 5.79 m² and 1.03 m²-24.57 m² with a mean of 4.64 m² for RTA and SPA,
460 respectively. The horizontal second moment of RTA is always larger than horizontal
461 second moment of SPA, indicating the PCE plume in aquifer of RTA is wider than PCE
462 plume in aquifer of SPA and RTA can cause larger range of groundwater contamination.
463 Similarly, the second moments in vertical direction of RTA are larger than the second
464 moments in vertical direction of SPA.

465 This study takes an important step toward exploring how micro-scale arrangements
466 control contaminant migration at small aquifer scale. Results are essential to the

macroscopic aquifer composed of porous media without large heterogeneity, such as sandy aquifers containing rich groundwater resources. However, upscaling problem of aquifer is widely existed in nature (Dagan et al., 2013; Pacheco, 2013; Pacheco et al., 2015). Due to large heterogeneity of natural aquifers, research results may be very different and can't be extrapolated to complex regional aquifer at large scale. On the other hand, the finding in this study is absolutely applicable for natural aquifers with similar heterogeneities. If the heterogeneity and anisotropy of natural aquifers are very different, the effect of the micro-scale arrangements on the macroscopic contaminant migration and remediation will be different. Even realistic conditions are complex, the new findings achieved from this research also is very significant for understanding micro-scale arrangements' effect on contaminant behaviors at aquifer scale. The upscaling problem of the results obtained at the simulation scale (100 x 25 x 25 m) is the basis and the upscaling problem with more complex heterogeneity conditions is needed to be further investigated. Various researches on upscaling problem are done from the aspects of experiment and simulation (Wu et al., 2017a, 2017b, 2017c, 2017d). Based on these research, the microstructure of porous media is developed and the contaminates migration in porous media are explored using fractal methods in this study, implying the experimental results are very significant for realistic problems at aquifer scale. Our next procedure is applying these models in realistic aquifer with complex heterogeneity conditions and modifying our models and method according to realistic conditions.

4. Conclusions

The micro-structure of aquifer has important effect on macroscopic scale

带格式的: 非加宽量 / 紧缩量

489 characteristics of aquifer and inner contaminant migration and remediation. In this study,
 490 we focus on the DNAPL migration and remediation in heterogeneous aquifer composed
 491 of granular porous media with RTA and SPA. The microscale models of RTA and SPA
 492 are developed to obtain the mathematical expressions of permeability and entry pressure
 493 using fractal method. 200 realizations of porosity field are generated using SGS method
 494 and PCE is released from underground storage tank into heterogeneous aquifer. To clean
 495 up contamination caused by underground storage tank spill, surfactant remediation
 496 technique is used to remove contaminants in aquifer. The entire process of DNAPL
 497 migration and remediation is simulated by a multicomponent, multiphase model
 498 simulator UTCHEM. Results suggest RTA not only cause larger range of groundwater
 499 contamination than RTA, but also the contaminated aquifer of RTA is harder to clean up
 500 compared with SPA. The second PCE plume moments in horizontal direction are 10.61
 501 m^2 -40.50 m^2 with a mean of 21.51 m^2 and 10.98 m^2 -36.38 m^2 with a mean of 20.75 m^2
 502 for 200 realizations based on RTA and SPA after PCE natural migration at $t=100$ day,
 503 respectively. Furthermore, the second PCE plume moments in horizontal direction at
 504 $t=300$ day are 0.807 m^2 -34.88 m^2 with a mean of 5.79 m^2 and 1.025 m^2 -24.57 m^2 with a
 505 mean of 4.64 m^2 for RTA and SPA respectively after long time remediation.
 506 Simultaneously, the residual DNAPL mass remained in aquifer are 0.67 m^3 -119.89 m^3
 507 with a mean of 22.42 m^3 and 0.79 m^3 -103.33 m^3 with a mean of 12.51 m^3 for RTA and
 508 SPA respectively, indicating remediation efficiency of SPA (65.53%-99.74% with a mean
 509 of 95.83%) mostly is higher than remediation efficiency of RTA (60.01%-99.78% with a
 510 mean of 92.52%). This study proves microstructure of aquifer has important effect on

511 contaminant movement and associated remediation efficiency in macroscopic scale
512 aquifer, which is very essential and significant for dealing with the accidental event of
513 underground storage tank spill and identifying subsurface contaminant source in the
514 future.

515 **Acknowledgments**

516 This research was financially supported by the National Key Research and
517 Development Plan of China (2016YFC0402807, 2016YFC0402802 and
518 2016YFC0402800), the National Natural Science Foundation of China-Xianjiang project
519 (U1503282), and the National Natural Science Foundation of China (41372235).

520 **References**

- 521 Ahn, K.J., Seferis, J.C.: Simultaneous measurements of permeability and capillary
522 pressure of thermosetting matrices in woven fabric reinforcements, Polym.
523 Composite., 12, 146-152, 1991.
- 524 Bakshevskaia, V.A., Pozdniakov, S.P., Simulation of hydraulic heterogeneity and
525 upscaling permeability and dispersivity in Sandy-Clay foormations, Math.
526 Geosci., 48, 45-64, 2016.
- 527 Bear, J.: Dynamics of fluids in porous media, Dover, New York, 1972.
- 528 Bob, M.M., Brooks, M.C., Mravik, S.C., Wood, A.L.: A modified light transmission
529 visualization method for DNAPL saturation measurements in 2-D models, Adv.
530 Water Resour., 31, 727-742, 2008.
- 531 Boswinkel, J.A.: International Groundwater Resources Assessment Centre (IGRAC),

532 Netherland Institute of Applied Geoscience, Netherlands, 2000.

533 Cui, Q.L., Wu, H.N., Shen, S.L., Yin, Z.Y., Horpibulsuk, S.: Protection of neighbour

534 buildings due to construction of shield tunnel in mixed ground with sand over

535 weathered granite, Environ, Earth Sci., 75, 458, 2016.

536 C.Carroll, K., McDonald, K., Marble, J., Russo, A.E., Brusseau, M.L.: The impact of

537 transitions between two-fluid and three-fluid phases on fluid configuration and

538 fluid-fluid interfacial area in porous media, Water Resour. Res., 51, 7189-7201,

539 2015.

540 Dagan, G., Fiori, A., Jankovic, I.: Upscaling of flow in heterogeneous porous formations:

541 Critical examination and issues of principle, Adv. Water Resour., 51, 67-85, 2013.

542 Dawson, H.E., Roberts, P.V.: Influence of Viscous, Gravitational, and Capillary Forces

543 on DNAPL Saturation, Groundwater, 35(2), 261-269, 1997.

544 Delshad, M., Pope, G.A., Sepehrnoori, K.: A compositional simulator for modeling

545 surfactant enhanced aquifer remediation, 1 Formation, J. Contam. Hydrol., 23,

546 303-327, 1996.

547 Eggleston, J.R., Rojstaczer, S.A., Peirce, J.J.: Identification of hydraulic conductivity

548 structure in sand and gravel aquifers: Cape Cod data set, Water Resour. Res., 32,

549 1209-1222, 1996.

550 Essaid, H.I., Bekins, B.A., Cozzarelli, I.M., Organic contaminant transport and fate in the

551 subsurface: Evolution of knowledge and understanding, Water Resour. Res., 51,

552 4861-4902, 2015.

553 Feng, Y.J., Yu, B.M.: Fractal dimension for tortuous streamtubes in porous media,

带格式的：两端对齐，缩进：悬挂缩进：3.36 字符，左
0.01 字符，首行缩进：-3.36 字符，定义网格后不调
整右缩进，不对齐到网格

554 Fractals, 15, 385-390, 2007.

555 Hadley, P.W., Newell, C.: The New Potential for Understanding Groundwater
556 Contaminant Transport, Groundwater, 52(2), 174-186, 2014.

557 Hu, K., White, R., Chen, D., Li, B., Li, W.: Stochastic simulation of water drainage at the
558 field scale and its application to irrigation management, Agr. Water Manage., 89,
559 123-130, 2007.

560 Huang, J.Q., Christ, J.A., Goltz, M.N., Demond, A.H.: Modeling NAPL dissolution
561 from pendular rings in idealized porous media, Water Resour. Res., 51, 8182-8197,
562 2015.

563 Katz, A.J., Thompson, A.H.: Fractal sandstone: Implications for conductivity and pore
564 formation, Phys. Rev. Lett., 54, 325-332, 1985.

565 Krohn, C.E.: Sandstone fractal and Euclidean pore volume distributions, J. Geophys.
566 Res., 93, 3286-3296, 1988.

567 Liang, C., Hsieh, C.L.: Evaluation of surfactant flushing for remediating EDC-tar
568 contamination, J. Contam. Hydrol., 177-178, 158-166, 2015.

569 Liang, C., Lai, M.C.: Trichloroethylene degradation by zero valent iron activated
570 persulfate oxidation, Environ. Eng. Sci., 25(7), 1071-1077, 2008.

571 Liu, H., Li, Y.X., He, X., Sissou, Z., Tong, L., Yarnes, C., Huang, X.: Compound-specific
572 carbon isotopic fractionation during transport of phthalate esters in sandy aquifer,
573 Chemosphere, 144, 1831-1836, 2016.

574 Liu, L.: Modeling for surfactant-enhanced groundwater remediation processes at
575 DNAPLs-contaminated sites, J. Environ. Inform., 5(2), 42-52, 2005.

576 Liu, L., Hao, R.X., Cheng, S.Y.: A possibilistic analysis approach for assessing
577 environmental risks from drinking groundwater at petroleum-contaminated sites,
578 J. Environ. Inform., 2(1), 31-37, 2003.

579 Liu, Y., Wang, S., McDonough, C.A., Khairy, M., Muir, D.C.G., Helm, P.A., Lohmann,
580 R.: Gaseous and freely-dissolved PCBs in the lower great lake based on passive
581 sampling: spatial trends and air-water exchange, Environ. Sci. Technol., 50,
582 4932-4939, 2016.

583 Pacheco, F.A.L.: Hydraulic diffusivity and macrodispersivity calculations embedded in a
584 geographic information system, Hydrolog. Sci. J., 58(4), 930-943, 2013.

585 Pacheco, F.A.L., Landim, P.M.B., Szocs, T.: Bridging hydraulic diffusivity from aquifer to
586 particle-size scale: a study on loess sediments from southwest Hungary, Hydrolog.
587 Sci. J., 60(2), 269-284, 2015.

588 Pfeifer, P., Avnir, D.: Chemistry in Nonintegral dimensions between two and three. I.
589 Fractal theory of heterogeneous surface, J. Chem. Phys., 79, 3558-3565, 1983.

590 Qin, X.S., Huang, G.H., Chakma, A., Chen, B., Zeng, G.M.: Simulation-based process
591 optimization for surfactant-enhanced aquifer remediation at heterogeneous
592 DNAPL-contaminated sites, Sci. Total Environ., 381, 17-37, 2007.

593 Schaefer, C.E., White, E.B., Lavorgna, G.M., Annable, M.D.: Dense nonaqueous-phase
594 liquid architecture in fractured bedrock: implications for treatment and plume
595 longevity, Environ. Sci. Technol., 50, 207-213, 2016.

596 Valipour, M.: Comparison of surface irrigation simulation models: Full hydrodynamic,
597 zero inertia, kinematic wave, J. Agr. Sci., 4(12), 68-74, 2012.

598 Valipour, M.: Future of agricultural water management in Africa, Arch, Agron. Soil Sci.,

带格式的：两端对齐，缩进：悬挂缩进：3.36 字符，左
0.01 字符，首行缩进：-3.36 字符，定义网格后不调
整右缩进，不对齐到网格

599 61(7), 907-927, 2015.

600 Valipour, M., Singh, V.P.: Global experiences on wastewater irrigation: challenges and
601 Prospects, in: Maheshwari, B., Singh, V.P., Thoradeniya, B., Balanced urban
602 development: options and strategies for liveable cities, Volume 72 of the series
603 Water Science and Technology Library, pp. 289-327, 2016.

604 Veneziano, D., Tabaei, A.: Nonlinear spectral analysis of flow through porous media with
605 isotropic lognormal hydraulic conductivity, J. Hydrol., 294, 4-17, 2004.

606 Weathers, T.S., Harding-Marjanovic, K., Higgins, C.P., Alvarez-Cohen, L., Sharp, J.O.:
607 Perfluoroalkyl acids inhibit reductive dechlorination of Trichloroethene by
608 repressing dehalococcoides, Environ. Sci. Technol., 50, 240-248, 2016.

609 Wu, M., Cheng, Z., Wu, J.F., Wu, J.C.: Quantifying representative elementary volume of
610 connectivity for translucent granular materials by light transmission
611 micro-tomography, J. Hydrol., 545, 12-27, 2017a.

612 Wu, M., Cheng, Z., Wu, J.F., Wu, J.C.: Estimation of representative elementary volume
613 for DNAPL saturation and DNAPL-water interfacial areas in 2D heterogeneous
614 porous media, J. Hydrol., 549, 12-26, 2017b.

615 Wu, M., Wu, J.F., Wu, J.C.: Simulation of DNAPL migration in heterogeneous translucent
616 porous media based on estimation of representative elementary volume, J. Hydrol.,
617 553, 276-288, 2017c.

618 Wu, M., Cheng, Z., Wu, J.F., Wu, J.C.: Precise simulation of long-term DNAPL
619 migration in heterogeneous porous media based on light transmission
620 micro-tomography, J. Environ. Chem. Eng. 5, 725-734, 2017d.

621 Yannopoulos, S.I., Lyberatos, G., Theodossiou, N., Li, W., Valipour, M., Tamburrino, A.,

622 Angelakis, A.N.: Evolution of water lifting devices (pumps) over the centuries
623 worldwide, *Water*, 7, 5031-5060, 2015.

624 Yu, B.M.: Fractal character for tortuous streamtubes in porous media, *CHIN. PHYS.*
625 *LETT.*, 22, 158-160, 2005.

626 Yu, B.M., Cai, J.C., Zou, M.Q.: On the physical properties of apparent two-phase fractal
627 porous media, *Vadose Zone J.*, 8, 177-186, 2009.

628 Yu, B.M., Cheng, P.: Fractal models for the effective thermal conductivity of bidispersed
629 porous media, *J. Thermophys. Heat Tr.*, 16, 22-29, 2002.

630 Yu, B.M., Li, J.H.: A geometry model for tortuosity of flow path in porous media, *CHIN.*
631 *PHYS. LETT.*, 21, 1569-1571, 2004.

632 Yun, M.J., Yu, B.M., Zhang, B., Huang, M.T.: A geometry model for tortuosity of
633 streamtubes in porous media with spherical particles, *CHIN. PHYS. LETT.*,
634 22(6), 1464-1467, 2005.

635

636 **Table 1.** Parameters used in simulation

Parameter	Value
Average value of porosity	0.22
Standard deviation of porosity	0.06
Longitudinal dispersivity	1.0 m
Transverse dispersivity	0.1 m
Hydraulic gradient	0.005 m/m
Water density	1.00 g/cm ³
PCE density	1.63 g/cm ³
Surfactant density	1.15 g/cm ³
Water viscosity	1.00 cp
PCE viscosity	0.89 cp
PCE/ Water interfacial tension	45 dyn/cm
PCE solubility in water	240 mg/L
Residual water saturation	0.24
Residual PCE saturation	0.17
Endpoint of Water (BC model)	0.486
Endpoint of PCE (BC model)	0.65
Exponent of Water (BC model)	2.85
Exponent of PCE (BC model)	2.7
Exponent of capillary pressure	-0.52

637

638

639 **Figure Captions**

640

641 **Figure 1.** Two different microscale arrangements of solid particles: (a) RTA; and (b)
642 SPA

643 **Figure 2.** Three kinds of Sierpinski gasket [30]: (a) $L_d=2$; (b) $L_d=3$; and (c) $L_d=5$

644 **Figure 3.** (a) Two-dimensional view of contaminated domain; and (b) locations of
645 injection extraction wells

646 **Figure 4.** (a) The individual porosity field generated by Sequential Gaussian Simulation
647 (SGS) method; (b) the frequency of individual porosity field; (c) the individual
648 permeability field of RTA obtained from individual porosity field; (d) the
649 frequency of individual permeability field for RTA; (e) the individual
650 permeability field of SPA obtained from individual porosity field; (f) the
651 frequency of individual permeability field for SPA; (g) The obtained individual
652 entry pressure field of RTA; (h) the frequency of individual entry pressure field
653 of RTA; (i) the obtained individual entry pressure field of SPA; and (j) the
654 frequency of individual entry pressure of SPA

655 **Figure 5.** Simulated PCE saturation for individual realization of RTA over the entire
656 migration and remediation periods (0~300 day)

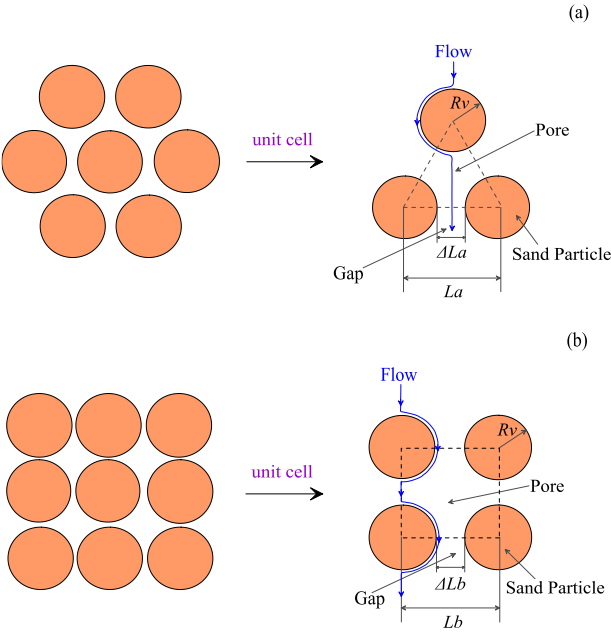
657 **Figure 6.** Simulated PCE saturation for individual realization of SPA over the entire
658 migration and remediation periods (0~300 day)

659 **Figure 7.** (a) PCE volume in aquifer versus time, RTA represents RTA and SPA
660 represents SPA; (b) Changes in GTP as a function of time; (c) Cumulative
661 DNAPL removal as a function of time; (d) Variation of GTP value as a function

662 of cumulative DNAPL removal percent; (e) the change of the center of PCE
663 plume during the entire periods of migration and remediation; (f) the change of
664 the depth of PCE plume center during the entire periods; (g) variation of second
665 PCE plume moment in horizontal axis; and (h) variation of second PCE plume
666 moment in vertical axis
667
668

669 **Figure 1**

670

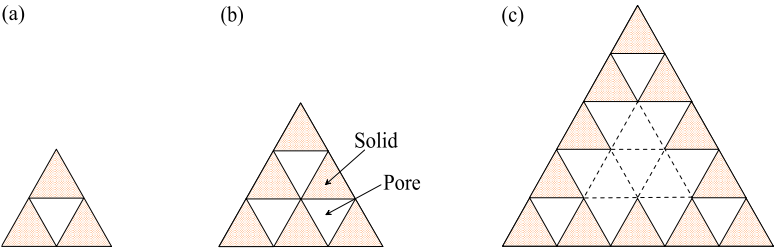


671

672

673 **Figure 2**

674



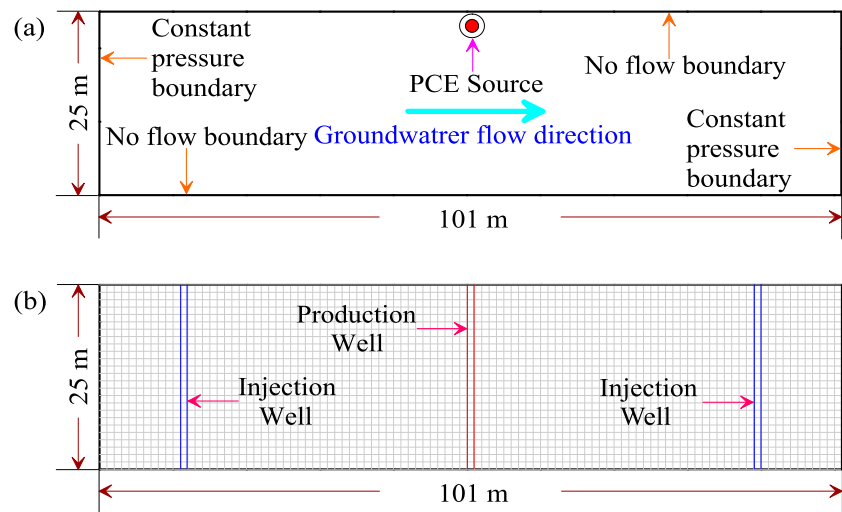
675

676

677

678 **Figure 3**

679



680

681

682 **Figure 4**

683

684

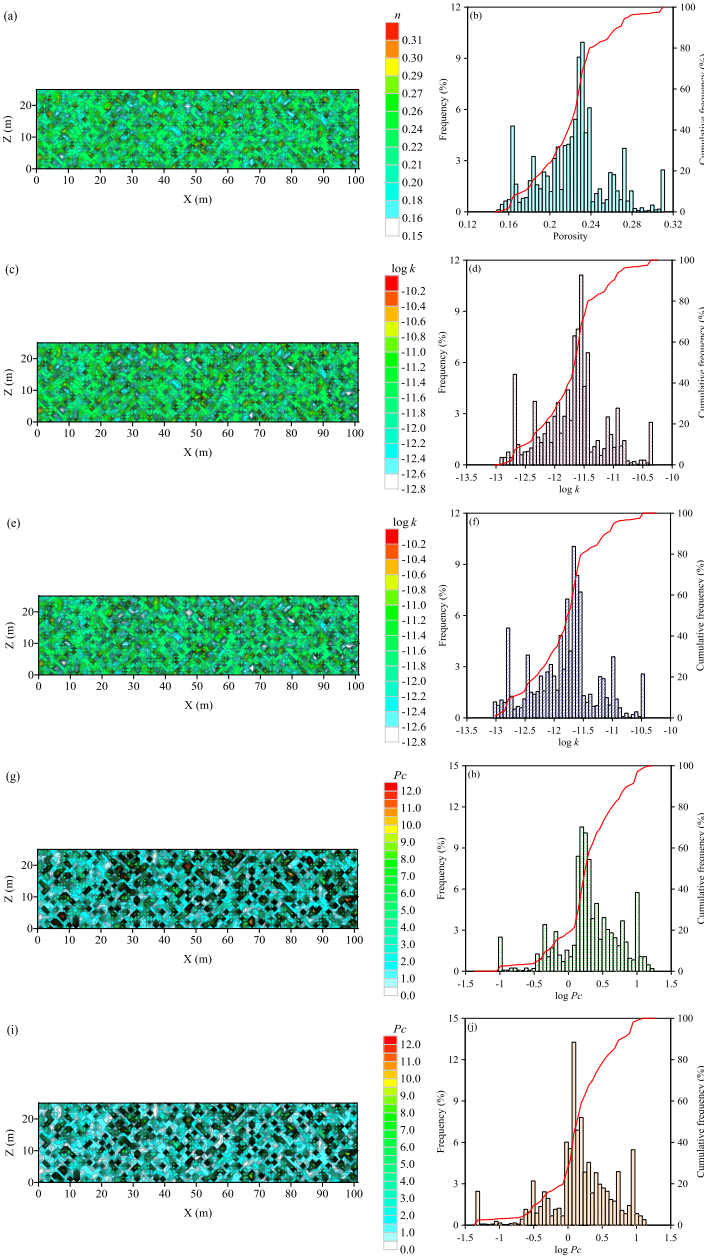
685

686

687

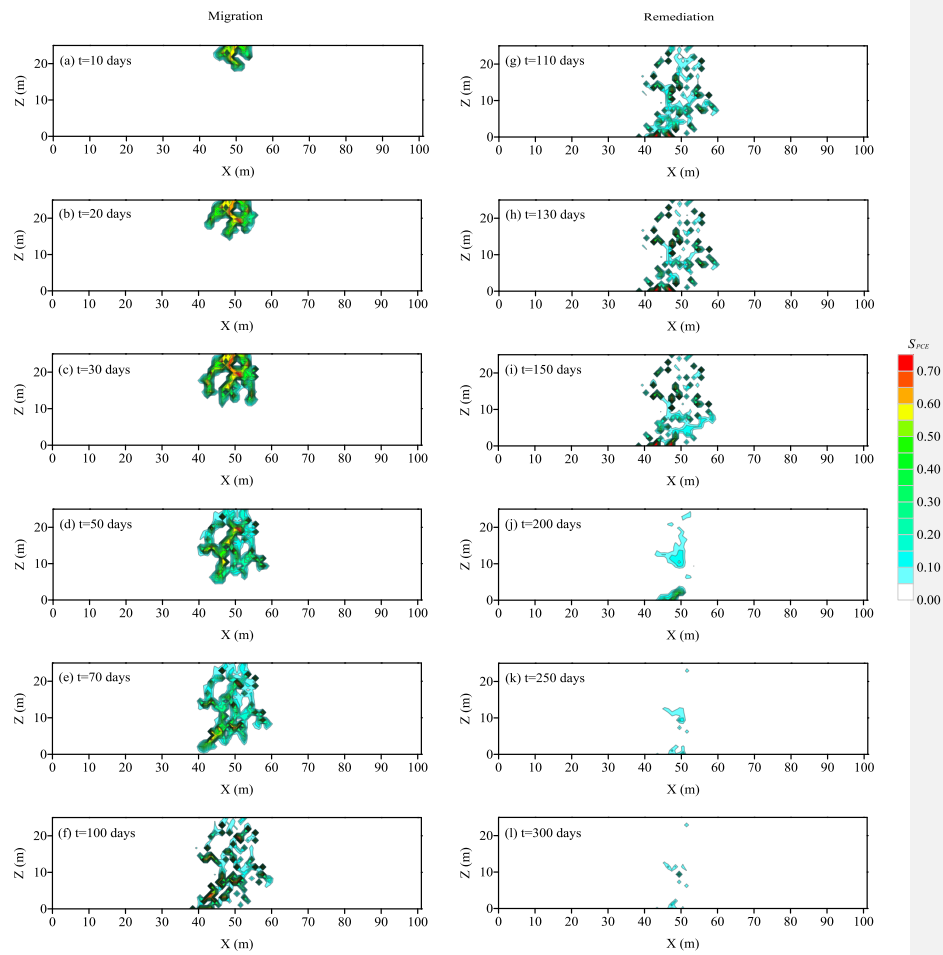
688

689



690 **Figure 5**

691

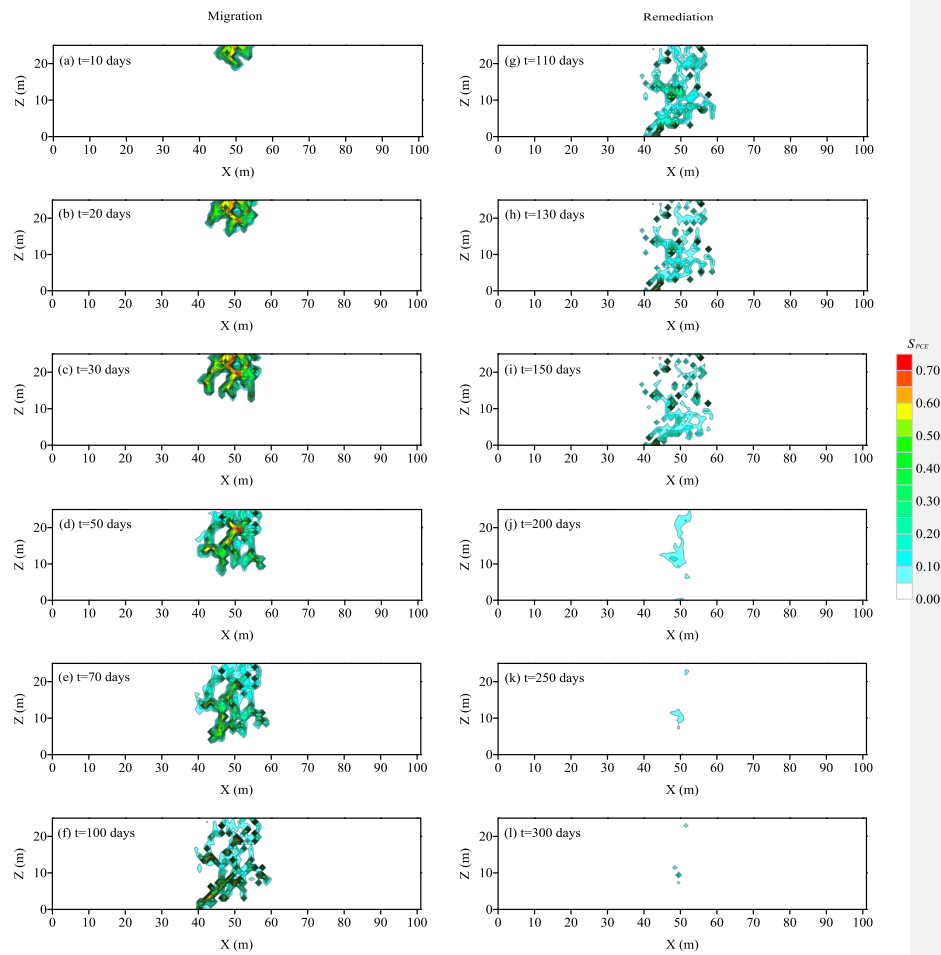


692

693

694 **Figure 6**

695

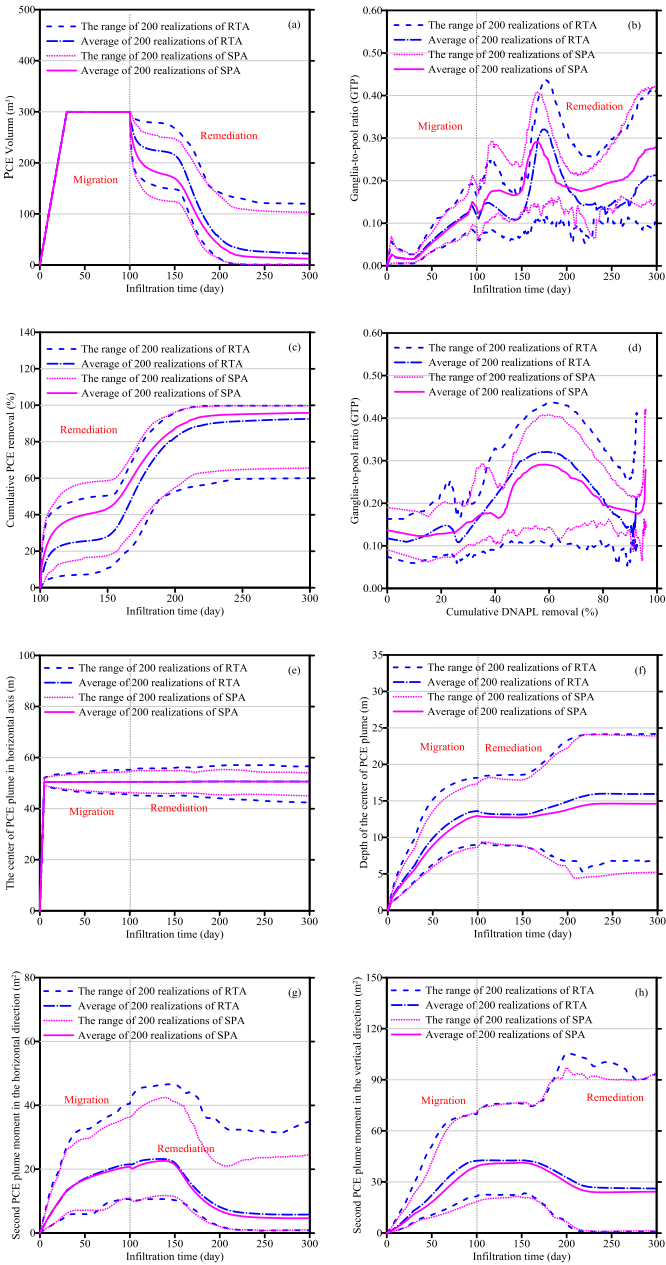


696

697

698 **Figure 7**

699



700